Macromolecules
ARTICLE

Macromolecules **2010**, *43*, 2453–2462 **2453**
DOI: 10.1021/ma902639g

Effects of Nanoscale Confinement and Pressure on the Dynamics of pODMA-*b*-p*t*BA-*b*-pODMA Triblock Copolymers

A. Gitsas,[†,∥] G. Floudas,*[,†] H.-J. Butt,[‡] T. Pakula,[‡] and K. Matyjaszewski[§]

[†]*University of Ioannina, Department of Physics, P.O. Box 1186, 451 10, Greece and Biomedical Research Institute (BRI-FORTH), Ioannina, Greece,* [‡]*Max-Planck Institut für Polymerforschung, 55128 Mainz, Germany, and* [§]*Center for Macromolecules Engineering, Department of Chemistry, Carnegie Mellon University, 4400 Fifth Avenue, Pittsburgh, Pennsylvania 15213.* [∥]*Present address: AIT Austrian Institute of Technology GmbH, Nano Systems, Donau-City-Strasse 1, 1220 Vienna, Austria.*

Received November 30, 2009; Revised Manuscript Received January 17, 2010

ABSTRACT: The effect of nanoscale confinement on the dynamics of a series of poly(*n*-octadecyl methacrylate)-*b*-poly(*tert*-butyl acrylate)-*b*-poly(*n*-octadecyl methacrylate) (pODMA-*b*-p*t*BA-*b*-pODMA) triblock copolymers, synthesized through atom transfer radical polymerization, has been investigated with dielectric spectroscopy as a function of temperature and pressure. The main effects of confinement were found in the triblocks with the more antisymmetric compositions when the radius of gyration of the confined block was comparable to the cylinder radius. It was found that the dynamics of the amorphous block accelerate upon confinement. Furthermore, confinement of the crystallizable block within cylindrical nanodomains results in the depression of the crystallization temperature.

I. Introduction

The behavior of polymers under confinement can be different from that of the bulk, especially when the molecules are confined to dimensions comparable to their size. For example, there are several reports for an enhanced segmental mobility in thin polymer films as a function of the film thickness,[1−3] in nanocomposites including polymer/layered silicates,[4,5] in suspended nanospheres[6] and under hard confinement (in nanoporous alumina).[7]

Block copolymers offer many possibilities for studying the effect of confinement on the dynamics. Block copolymers can be synthesized with a precise control of the interfacial curvature and nanodomain size by varying, respectively, the composition and block lengths.[8] Furthermore, utilizing block copolymers comprising both amorphous and crystallizable blocks allows us to investigate the effect of confinement on the segmental dynamics as well as on the crystallization process. In addition, recent progress mainly with dielectric spectroscopy (DS) techniques made possible the investigation of the dynamics of glass-forming liquids,[9] amorphous polymers,[10] and liquid crystals[11,12] as well as of the phase transitions under pressure.[11,13,14] However, to our knowledge, there exists only one investigation[15] of the influence of pressure on the dynamics of phase-separated block copolymers. In block copolymers of poly(methyl vinyl ether) with poly(isobutyl vinyl ether), increasing pressure was found to have a much stronger effect than decreasing temperature because of the dynamic asymmetry of the two homopolymers forming the blocks.[15]

Recently, we reported[16] on the phase behavior of triblock copolymers poly(*n*-octadecyl methacrylate)-*b*-poly(*tert*-butyl acrylate)-*b*-poly(*n*-octadecyl methacrylate) (pODMA-*b*-p*t*BA-*b*-pODMA) in bulk and on surfaces using small-angle X-ray scattering (SAXS) and atomic force microscopy (AFM), respectively. p*t*BA is an amorphous polymer with a glass temperature (T_g) of 316 K, whereas pODMA undergoes side-chain crystallization below ∼285 K (with a melting temperature (T_m) of 300 K). X-ray measurements within the disordered state identified the interaction parameter and its (strong) temperature dependence ($\chi = 0.12 + 38/T$). On the basis of the $\chi(T)$, it was shown that the majority of the copolymers are in the strong segregation limit (SSL), as demonstrated by the values of the product of the interaction parameter with the total degree of polymerization $\chi N \approx 100$. The phase diagram consists of a majority lamellar phase, with smaller regions of hexagonally packed cylindrical and cubic phases.[16] This system is ideal for studying the effect of confinement on the dynamics because it is composed of both amorphous and crystallizable blocks. Depending on composition, either the amorphous or the crystallizable block can be confined within cylindrical or spherical nanodomains. In addition, it is not known how pressure affects the thermodynamic and dynamic properties of the two blocks.

Herein we employ the same series of pODMA-*b*-p*t*BA-*b*-pODMA triblock copolymers and investigate the effect of confinement on the dynamics as well as on the thermodynamics of the two blocks forming the nanophases. We start the investigation by considering the homopolymers. By using pressure as an additional thermodynamic parameter, we first identify the main control parameter associated with the liquid-to-glass transition. Subsequently, we employ four triblock copolymers denoted as S14, S52, S81, and S94, with respective pODMA volume fractions of 0.14, 0.52, 0.81, and 0.94. The nanophase structure in S14 consists of pODMA hexagonally packed cylinders confined by the glassy p*t*BA matrix; S52 has a lamellar nanophase; in S81 (S94), glassy cylinders (spheres) of p*t*BA are confined by crystallizable pODMA forming the matrix. As with the homopolymers, we employ pressure in addition to temperature and investigate the glass and crystallization temperatures at elevated pressures by employing temperature- and pressure-dependent DS. We find that confinement affects both the dynamics of the confined amorphous block and the thermodynamic properties of the crystallizable block.

*Corresponding author. E-mail: gfloudas@cc.uoi.gr.

Published on Web 02/15/2010

Table 1. Molecular Characteristics of the pODMA-*b*-p*t*BA-*b*-pODMA Triblock Copolymers and the Homopolymers

sample	M_n (total) (g/mol)[a]	M_n (pODMA) (g/mol)[a]	M_n (p*t*BA) (g/mol)[a]	wt (%) (pODMA)	f_{pODMA}[b]	M_w/M_n
p*t*BA	82 800		82 800			1.10
S14	94 900	11 400	83 500	0.12	0.14	1.18
S52	105 200	50 500	54 700	0.48	0.52	1.17
S81	108 800	84 900	23 950	0.78	0.81	1.15
S94	124 200	115 500	8700	0.93	0.94	1.35
pODMA	143 000	143 000		1.00	1.00	2.40

[a] NMR. [b] $\rho_{pODMA} = 0.858$ g/cm^3; $\rho_{ptBA} = 1$ g/cm^3.

II. Experimental Section

Materials and Characterizations. The synthesis of the triblock copolymers series through atom transfer radical polymerization (ATRP) has been previously described.[17−19] The molecular characteristics of the copolymers used herein are tabulated in Table 1.

Differential Scanning Calorimetry (DSC). A Mettler Toledo Star DSC capable of programmed cyclic temperature runs over the range of 113−673 K was used. The samples were first heated at a rate of 10 K·min^{-1} from ambient temperature to 473 K and then cooled to 200 K with the same rate. In all samples, pODMA underwent side-chain crystallization upon cooling at a crystallization temperature (T_c) of ∼285 K.[13] The apparent melting temperature (T_m) was at ∼305 K, that is, below the glass temperature of p*t*BA ($T_g^{ptBA} = 316$ K).

Rheology. An advanced rheometric expansion system (ARES) equipped with a force-rebalanced transducer was used in the oscillatory mode for the p*t*BA homopolymer. Depending on the temperature range, two transducers were used with 2000 (2 g·cm) and 200 (0.2 g·cm) upper and lower sensitivity, respectively. The p*t*BA sample was prepared on the lower plate of the 10 mm diameter parallel plate geometry setup and heated under a nitrogen atmosphere until it could flow. Subsequently, the upper plate was brought into contact, the gap thickness was adjusted to 1 mm, and the sample was slowly cooled to the desired starting temperature. For the lower temperatures investigated (near the glass temperature) plates with 6 mm diameter were employed, and the strain amplitude was typically 0.05%. The storage (G') and loss (G'') shear moduli were monitored in different types of experiments. First, the linear and nonlinear viscoelastic ranges were identified by recording the strain amplitude dependence of the complex shear modulus $|G^*|$ at selected temperatures. In the subsequent experiments, strain amplitudes within the linear viscoelastic range were used. These experiments involved isothermal frequency scans for temperatures in the range of 319−403 K and for frequencies $10^{-2} < \omega < 10^2$ rad/s.

Pressure−Volume−Temperature (*PVT*). *PVT* measurements were carried out in the p*t*BA homopolymer ($M_w = 82\,000$ g/mol) with a Gnomix dilatometer using the confining fluid technique (A. Best, MPI-P). The sample was immersed in mercury, and the combined volume changes were measured. We determined the volume changes in the sample by subtracting the known volume change of mercury. Measurements were made under "isothermal" conditions for pressures in the range from 0.1 to 200 MPa and for temperatures in the range from 295 to 460 K.

Dielectric Spectroscopy. Dielectric measurements were made under "isobaric" conditions as a function of temperature and under "isothermal" conditions as a function of pressure. All measurements were performed using a Novocontrol BDS system composed of a Solartron Schlumberger FRA 1260 frequency response analyzer and a broadband dielectric converter for the range of 10^{-2} to 10^6 Hz. The temperature for the atmospheric pressure measurements was stabilized by a Novocontrol Quatro cryosystem with N_2 flow and a precision of 0.05 K. The "isobaric" measurements were performed at different temperatures in the range of 123−390 K at atmospheric pressure. The "isothermal" measurements were made for temperatures in the range from 298 to 363 K and for pressure up to 300 MPa. The measurements under hydrostatic pressure were carried out in a Novocontrol pressure cell.[20] The pressure setup consists of a temperature-controlled cell, hydraulic closing press with air pump, and air pump for hydrostatic test pressure. The sample cell is isolated with a Teflon ring from the surrounding silicone oil that is the pressure-transmitting liquid. The "isothermal" frequency sweeps were made with a temperature stability better than ±0.1 K and a pressure stability better than ±2 MPa.

In every case, the complex dielectric permittivity, $\varepsilon^* = \varepsilon' - i\varepsilon''$, where ε' is the real and ε'' is the imaginary part, was obtained as a function of angular frequency, ω, temperature, T, and pressure, P; that is, $\varepsilon^*(T,P,\omega)$.[10] The analysis of both T- and P-dependent experiments was made using the empirical equation of Havriliak and Negami (HN)[21]

$$\varepsilon^*(T,P,\omega) = \varepsilon_\infty(T,P) + \frac{\Delta\varepsilon(T,P)}{[1+(i\omega\tau_{HN}(T,P))^m]^n} + \frac{\sigma_0(T,P)}{i\varepsilon_f\omega} \quad (1)$$

where $\varepsilon_\infty(T,P)$ is the high-frequency permittivity, $\tau_{HN}(T,P)$ is the characteristic relaxation time in this equation, $\Delta\varepsilon(T,P) = \varepsilon_o(T,P) - \varepsilon_\infty(T,P)$ is the relaxation strength, m, n (with limits $0 < m$, $mn \le 1$) describe, respectively, the symmetrical and asymmetrical broadening of the distribution of relaxation times, σ_0 is the dc conductivity, and ε_f is the permittivity of free space. From τ_{HN}, the relaxation time at maximum loss, τ_{max}, is obtained analytically following

$$\left[\sin\left(\frac{\pi m}{2+2n}\right)\right]^{1/m}\tau_{max} = \tau_{HN}\left[\sin\left(\frac{\pi mn}{2+2n}\right)\right]^{1/m} \quad (2)$$

The electric modulus, $M^*(\omega)$, is related with the dielectric function $\varepsilon^*(\omega)$ through

$$M^*(\omega) = \frac{1}{\varepsilon^*(\omega)} = M' + iM'' \quad (3)$$

where M' and M'' are the real and imaginary parts of the electric modulus, respectively. The electric modulus representation, rather than the dielectric function, has been proposed not only for systems containing a substantial concentration of mobile carriers but also for any dielectrically active process. This representation can also be used to extract the ionic mobility from the crossing of the real and the imaginary part. The relaxation times from the maximum of ε'' and M'' are related through $\tau_{M''} = \tau_{\varepsilon''}(1+\Delta\varepsilon/\varepsilon_\infty)^{-1/m}$, in the case of a symmetric distribution; that is, $n = 1$.[22,23] Hence, it is only for weak processes that the two times coincide. At high temperatures, the derivative of ε' ($d\varepsilon'/d \ln \omega \approx -(2/\pi)\varepsilon''$) has been used to avoid the conductivity contribution.[24]

III. Results and Discussion

Thermodynamic Properties. The side-chain crystallization of pODMA has been previously explored as a function of

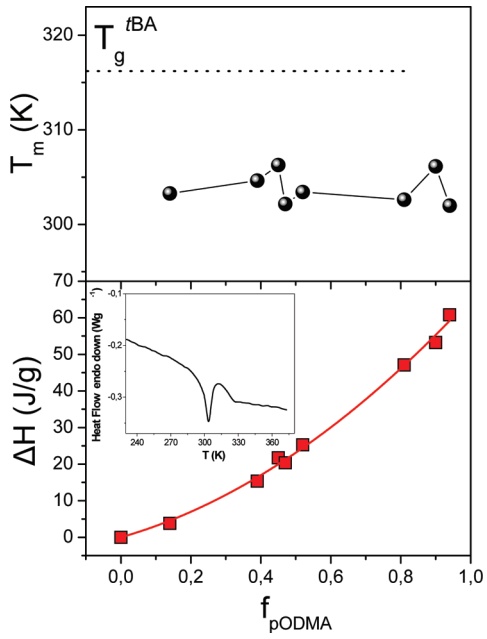

Figure 1. Dependence of the apparent melting temperature, T_m, of the pODMA block (top) and heat of fusion, ΔH, (bottom) on copolymer composition. The melting temperature remains practically unchanged, whereas the observed heat of fusion follows a nonlinear dependence because of the block copolymer nature of the system. In the inset, the DSC trace of the copolymer S14 (rate 10 K·min^{-1}) during the second heating run is shown. The melting of pODMA corresponds to the endothermic peak, whereas the glass temperature of p*t*BA can be observed in S14 as a step in heat capacity.

temperature and pressure.[13] In addition, the kinetics of side-chain crystallization were found to deviate from the normal Avrami kinetics[13] (i.e., fractional exponents were found). The thermal investigation (DSC) explored the side-chain crystallization of the semicrystalline (pODMA) as well as the liquid-to-glass transition of the amorphous block (p*t*BA), in the copolymers. The pODMA melting temperature in the copolymers (T_m^{pODMA}) does not vary considerably for the investigated compositions, being in the range 304 ± 3 K, suggesting a constant crystal thickness. The melting temperature at peak heat flow is plotted in Figure 1 together with the corresponding heats of fusion (ΔH) as a function of copolymer composition. The dependence of ΔH on composition is nonlinear, and the composition dependence can be fitted with an empirical polynomial function: $\Delta H = 37f + 26f^2$ (J/g), where f is the pODMA volume fraction in the triblocks. The nonlinear dependence suggests some effects of the interfaces on the ability of alkyl chains in pODMA to crystallize. The glass temperature of the amorphous block (p*t*BA), observed as a step in the heat capacity (inset in Figure 1) at ~316 K, can clearly be resolved in the triblock where p*t*BA is the majority component (S14). Additional DSC curves are included in Figure S1 of the Supporting Information. In triblocks with >14% in pODMA, the endothermic peak overlaps with the T_g^{ptBA}, making the deconvolution a difficult task (although it is possible to decouple the two effects by temperature-modulated DSC). Despite this, the T_g^{ptBA} from S14 is included in Figure 1 as a straight line at T=316 K, for comparison. The analysis of the DS data (below), can provide the glass temperature of p*t*BA in the copolymers unambiguously. As we will see below, the p*t*BA glass temperature is practically identical to the homopolymer value for all copolymers except the one rich in pODMA (S81). In this case, a lower T_g value was found and is subsequently discussed.

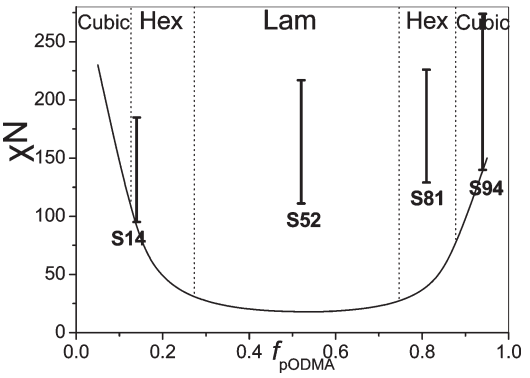

Figure 2. Phase state diagram based on the results from the structural investigation. The dashed lines give the approximate positions of phase boundaries. The vertical bars correspond to the temperature range of the DS investigation (123−370 K) for the different block copolymer compositions employed in the present study, resulting in the different χN values shown. The curved solid line that separates the ordered from the disordered regions is the prediction from the mean-field theory.

The positioning of the investigated samples in the mean-field phase diagram is shown in Figure 2. The phase diagram is dominated by the lamellar phase, with smaller regions of hexagonally packed cylindrical and cubic phases. All copolymers are within the SSL ($\chi N \approx 100$). This ensures the absence of segmental mixing within the temperature range investigated by DS. The vertical bars indicate the χN range investigated by varying the temperature in the DS measurements. Of particular interest for the present investigation are the copolymers S14 and S81, with nearly antisymmetric composition; in the former, the crystallizable block is confined within the cylindrical domains, whereas in the latter, it is the amorphous blocks that are confined.

Homopolymer Dynamics. The components of the electric modulus (M' and M'') measured within the temperature range 317 ≤ T ≤ 360 K and of the shear modulus (G' and G'') measured within the temperature range 319 ≤ T ≤ 403 K, are compared in Figure 3 at the same (reference) temperature (T_r = 329 K). In the Figure, the frequency axes have been multiplied by appropriate shift factors (a_T) at each temperature so as to bring the loss modulus maxima for the segmental (α) process in coincidence with the loss maximum of T_r. The vertical axes in the electric modulus representation have also been shifted by corresponding factors b_T and c_T. The horizontal shift factors can be described by the well-known Williams−Landel−Ferry (WLF) equation: $\log a_T = -c_1^r(T - T_r)/(c_2^r + (T - T_r))$, where c_1^r and c_2^r are the WLF parameters at the reference temperature. The values of the above parameters at the glass temperature, T_g, can be recalculated as: $c_1^g = c_1^r c_2^r/(c_2^r + T_g - T_r)$ (= 12.7) and $c_2^g = c_2^r + (T_g - T_r)$ (= 41 K). Two main processes are seen on the master curve of the electric modulus: the segmental process and the ion mobility process at higher and lower frequencies, respectively. In the shear moduli representation, the segmental and chain (terminal) processes contribute at high and lower frequencies, respectively. As expected for a terminal flow, the low frequency slopes in the double logarithmic plot of G' and G'' are 2 and 1, respectively; (tTs) works approximately only around the segmental (α) process maximum. At higher and lower frequencies, the superposition fails because of the presence of a "fast" β-process and of a "slower" component associated with the ion mobility with distinctly different T-dependencies. In addition, as we will discuss below, the segmental process splits into two processes at higher temperatures (called α and α′), and this is the main reason for the failure of tTs around the segmental peak at

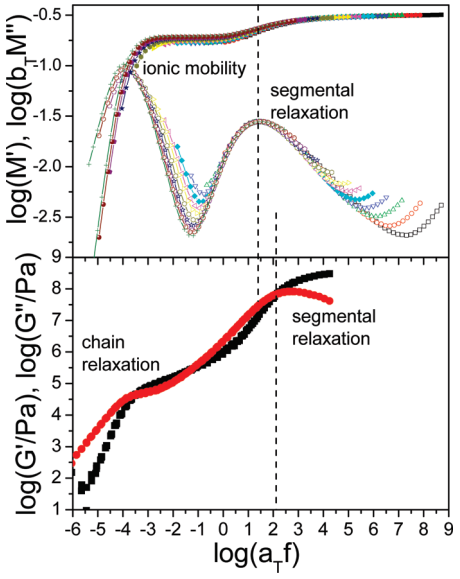

Figure 3. Comparison of the superimposed electric modulus, M^* (T range: 317−350 K) (top: open symbols, M''; filled symbols: M'), and of the mechanical shear modulus G^* (bottom: ■, G'; ●, G''), at the same reference temperature (T_r = 328 K) (T range 319−403 K) for p*t*BA plotted as a function of reduced frequency. The time−temperature superposition (*t*Ts) holds simultaneously for the segmental and the chain relaxation processes only in the mechanical spectra. Vertical lines indicate the position of the segmental process as obtained from the electric and shear moduli. At low frequencies, the storage and loss moduli can be described by $\log G'' = 8.3 + \log f$ and $\log G' = 12.1 + 2\cdot\log f$, respectively, and are associated with the chain (terminal) relaxation.

higher temperatures. The superposition of viscoelastic properties works satisfactory as a result of the smaller frequency range accessible by rheology.

The dielectric loss curves were fitted to the HN equation, and at each temperature and pressure, four parameters were extracted ($T\Delta\varepsilon$, m, n, and τ) associated, respectively, with the dielectric strength, the shape of the process, and the characteristic relaxation time. For the α process, the products of temperature with the dielectric strength, $\Delta\varepsilon$, $T\Delta\varepsilon$ are 670 ± 70 and 900 ± 40 K, and the shape parameters are $m = 0.85 \pm 0.01$, $n = 0.23 \pm 0.03$ and $m = 0.73 \pm 0.01$, $n = 0.44 \pm 0.01$ at temperatures higher and lower than the splitting temperature, respectively. The faster α′ process is much weaker with $T\Delta\varepsilon = 100 \pm 10$ K, $m = 0.75 \pm 0.10$, and $n = 1$. The process associated with the ionic mobility has $T\Delta\varepsilon = 370 \pm 80$ K, $m = 0.97 \pm 0.01$, and $n = 1$; that is, it is nearly a Debye process.

In Figure 4, the dielectric and rheology relaxation times for the different processes are plotted against inverse temperature in the usual Arrhenius representation and fitted with the Vogel−Fulcher−Tammann (VFT) equation

$$\tau_{max} = \tau_0 \exp \frac{D_T T_0}{T - T_0} \qquad (4)$$

where T_0 is the ideal glass temperature, τ_0 is the relaxation time in the very high-temperature limit, and D_T a dimensionless parameter. Notice that α′ merges with the α process by decreasing temperature and that the ion mobility process in DS is coupled to the polymer terminal relaxation. The latter, however, is not always the case, because the process of ionic conductivity also depends on the ion concentration in addition to the ion mobility. Table 2 provides the VFT parameters of all processes. For lower temperatures, the relaxation times corresponding to the β process are plotted,

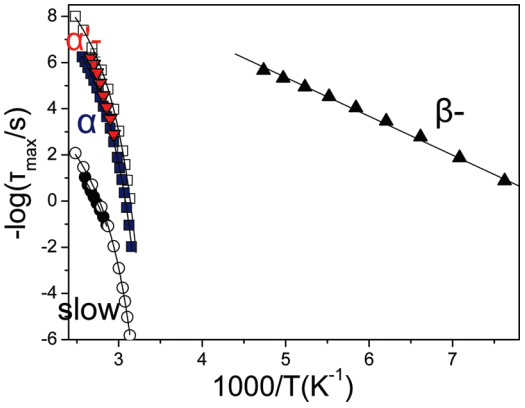

Figure 4. Dielectric (filled symbols) and rheology (open symbols) relaxation times of p*t*BA, as obtained from Figure 3, plotted in the usual Arrhenius representation and fitted with the VFT equation. Notice that the dielectric α (■) and α′ (▼) processes merge by decreasing temperature. The slow process in DS (●), due to the ion mobility, is coupled to the terminal relaxation from rheology. A dielectrically active β process (▲) at low temperatures, with an Arrhenius temperature dependence, is also included in this plot.

Table 2. VFT Parameters of the Main p*t*BA Processes

process	$-\log(\tau_0/s)$	D_T	T_0 (K)	T_g (K)
α (G'')	12.1 ± 0.1	4.5 ± 0.1	274 ± 1	311 ± 1
α (ε''_{der})	11.1 ± 0.1	4.8 ± 0.1	274 ± 1	316 ± 1
slow (G''/G' crossing)	6.4 ± 0.1	4.5 ± 0.1	274 ± 1	
slow (ε''_{der})	5.6 ± 0.1	4.8	268 ± 1	

as obtained from DS. This process shows an Arrhenius temperature dependence

$$\tau_{max} = \tau_0 \exp\left(\frac{E}{RT}\right) \qquad (5)$$

where $\tau_0 \approx 10^{-14}$ s and E is the apparent activation energy (32.2 ± 0.4 kJ/mol) and correspond to a localized dipolar relaxation at temperatures below the α process.

Pressure provides additional information on the dynamic processes from the $\tau(P)$ dependence that associate with an additional thermodynamic parameter, namely, the apparent activation volume,[10] $\Delta V^{\#}$, reflecting the sensitivity of the dynamics to pressure. The dielectric loss curves of p*t*BA as a function of frequency under "isobaric" and "isothermal" conditions at P = 0.1 MPa and at T = 363 K, respectively, are shown in Figure 5. The curves are obtained from the derivatives of the ε' and display the dual α and α′ processes at higher frequencies and a peak at lower frequencies associated with the ion mobility. Figure S2 of the Supporting Information provides a representative fit using a single and a double HN function that justifies the need for the additional faster process. Notice that the α′ process separates from the main α process only at low pressures and high temperatures. In all other cases, it is coupled to the α process and gives rise to a single glass temperature. The α′ process is a local relaxation that can be attributed to the deprotection of few *t*-Bu groups in p*t*BA.[25] We mention here that recent NMR studies on the structural relaxation of poly(*n*-alkylmethacrylates) revealed extended chain segments comprising 5−10 repeat units.[26] The randomization/isotropization of these segments gives rise to a dynamic process that is longer than the fast axial reorientation associated with the dielectric α process. The peak at lower frequencies reflects the process of ionic conductivity. The latter was found to depend on the (T, P) history, as discussed earlier.[23,27]

The corresponding "isothermal" relaxation times of the three processes, recorded with increasing pressure, are

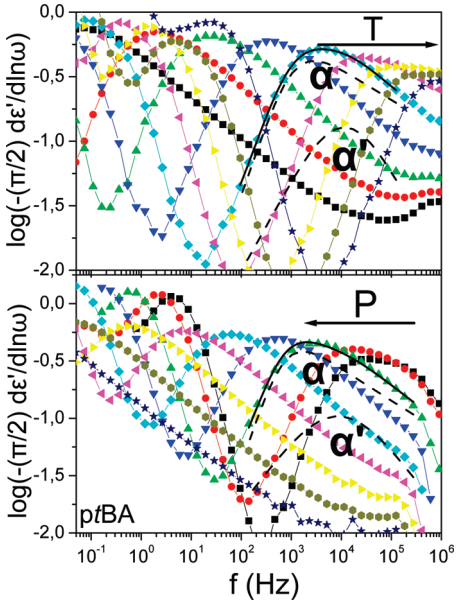

Figure 5. Dielectric loss of p*t*BA (obtained from the derivative method) as a function of frequency under "isobaric" (top, $P = 0.1$ MPa) and "isothermal" (bottom, $T = 363$ K) conditions. Temperature and pressure increase in the direction of the arrows: (top) $T = 320$ (■), 326 (●), 332 (▲), 340 (▼), 350 (◆), 360 (left triangles), 370 (right triangles), 380 (⬢), and 390 K (★); (bottom) $P = 0.1$ (■), 10 (●), 30 (▲), 50 (▼), 70 (◆), 90 (left triangles), 110 (right triangles), 130 (⬢), and 150 MPa (★), respectively. An example of fitting the segmental process with two HN equations, corresponding to the α and α′ processes (dashed lines), is shown in both representations.

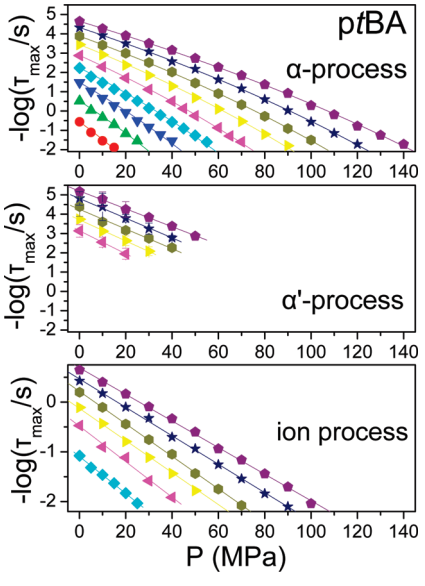

Figure 6. Segmental relaxation times of the α (top), α′ (middle), and slow (bottom) processes of p*t*BA as a function of pressure at different temperatures: $T = 323$ (●), 328 (▲), 333 (▼), 338 (◆), 343 (left triangles), 348 (right triangles), 353 (⬢), 358 (★), and 363 K (pentagons), respectively. The data of the α process have been fitted with the modified VFT equation, whereas a linear fit to α′ and slower processes is adequate given the smaller accessible frequency range.

presented in Figure 6. The relaxation times of the α process display a steep $\tau(P)$ dependence that conforms to the pressure equivalent[28] of VFT as

$$\tau_{max} = \tau_\alpha \exp \frac{D_P P}{P_0 - P} \tag{6}$$

where τ_α is the segmental relaxation time at atmospheric pressure at a given temperature, D_P (= 53) is a dimensionless parameter, and P_0 is the pressure corresponding to the ideal glass. A linear $\tau(P)$ dependence suffices to describe the α′ and the ion processes as a result of the smaller frequency range available for these processes. The apparent activation volume, $\Delta V^\#$, of the three processes (α, α′, and ion mobility) is presented in Figure S3 of the Supporting Information. As anticipated, the apparent activation volume is slightly higher for the α′ process as compared with the α process, but both show the same increase on approaching the T_g[10] (unlike that of the ion mobility process). The relative contribution of the available thermal energy and volume to the dynamic processes will be discussed below.

Relative Contribution of Temperature and Volume to the Homopolymer Dynamics. Identifying the main control parameter that dominates the slow dynamics in glass-forming liquids that give rise to the dynamic arrest at T_g has been a point of debate for many years. Theoretical predictions consider two extreme cases: thermally activated processes on a constant density "energy landscape"[29] and free-volume theories.[30] In the former picture, the controlling parameter is temperature, the landscape is considered as fixed, and the strong $\tau(T)$ is attributed to changes in the barriers and the minima encountered in the exploration of the landscape. In the latter picture, the controlling parameter is volume (V) or density (ρ), and the slowing-down results from the decrease in the available or "free" volume. Clearly, these pictures should be considered as extreme cases because molecular transport, in general, is driven by thermal activation processes with potential energy barriers that depend on local density.[31] Pressure-dependent measurements have been of paramount importance in the effort to disentangle the effects of T and ρ on the dynamics because pressure can be applied isothermally (affecting only ρ).

A critical test of the origin of the different dynamic processes and an assessment of the relative influence of volume and temperature in each case is provided by the value of the ratio of the apparent activation energy at constant volume, $Q_V(T,V) = R(\partial \ln \tau/\partial(1/T))_V$, to that at constant pressure, $Q_P(T,P) = R(\partial \ln \tau/\partial(1/T))_P$

$$Q_V(T,V)/Q_P(T,P) = (\partial \ln \tau_\alpha/\partial(1/T)_V)/(\partial \ln \tau_\alpha/\partial(1/T)_P) \tag{7}$$

This ratio assumes values in the range of 0 to 1 and provides a quantitative measure of the role of temperature and density on the dynamics. Ideally, values near unity suggest that the dynamics are governed mainly by the thermal energy, whereas values near zero suggest that free volume ideas prevail because in that case, $Q_V = 0$. Williams derived[32] an extension of the Eyring transition state theory for chemical reactions for application to structural relaxation in polymers that gave the following equations

$$\begin{aligned} -RT^2(\partial \ln \tau/\partial T)_P &= \Delta H^\#(T,P) + RT/2 \\ -RT^2(\partial \ln \tau/\partial T)_V &= \Delta E^\#(T,V) + RT/2 \\ (\partial \ln \tau/\partial P)_T &= \Delta V^\#(T,P)/RT \end{aligned} \tag{8}$$

where $\Delta H^\#$, $\Delta E^\#$, and $\Delta V^\#$ are, respectively, the "activation enthalpy", "activation internal energy", and "activation volume", defined with respect to unactivated and activated standard states of a relaxor. Therefore, the ratio $Q_V(T,V)/Q_P(T,P)$

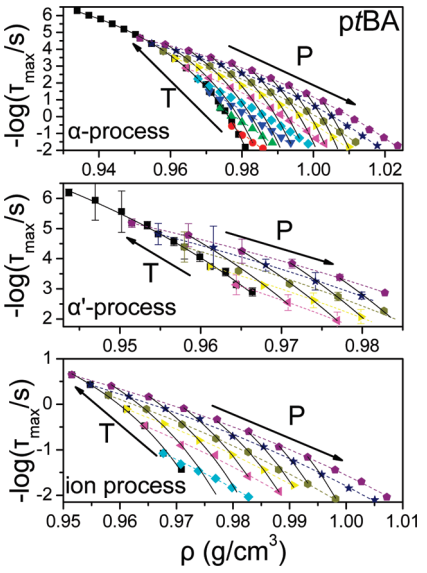

Figure 7. Segmental relaxation times of the α (top), α′ (middle), and the slower process (bottom) of p*t*BA as a function of density. The lines are fits of the modified VFT equation. Top: isothermal, $D_\rho^T = 2.96$, ---; $T =$ 323 (●), 328 (▲), 333 (▼), 338 (◆), 343 (left triangles), 348 (right triangles), 353 (⬢), 358 (★), and 363 K (pentagons); isobaric, $D_\rho^P =$ 0.89, —; $0.1 < P < 90$ MPa in 10 MPa increments; ■, $P = 0.1$ MPa). Middle: isothermal, $D_\rho^T = 3.9$, ---; $T = 343$ (left triangles), 348 (right triangles), 353 (⬢), 358 (★), and 363 (pentagons); isobaric, $D_\rho^P = 1.8$, —; $0.1 < P < 70$ MPa in 10 MPa increments; ■, $P = 0.1$ MPa). Bottom: isothermal, $D_\rho^T = 2.65$, ---; $T = 338$ (◆), 343 (left triangles), 348 (right triangles), 353 (⬢), 358 (★), and 363 K (pentagons); isobaric, $D_\rho^P =$ 0.38, —; $0.1 < P < 70$ MPa in 10 MPa increments; ■, $P = 0.1$ MPa).

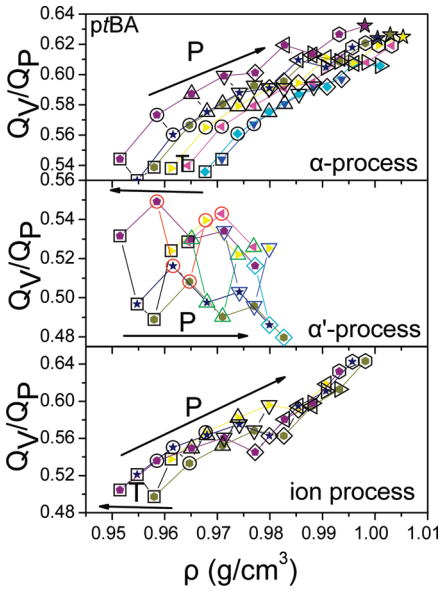

Figure 8. T and P dependence of the ratio of activation energies Q_V/Q_P for the α (top), α′ (middle), and the slow process (bottom). Top, solid symbols: $T = 333$ (▼), 338 (◆), 343 (left triangles), 348 (right triangles), 353 (⬢), 358 (★), and 363 K (pentagons); open symbols: $P = 0.1$ (□), 10 (○), 20 (△), 30 (▽), 40 (◇), 50 (left triangles), 60 (right triangles), 70 (⬡), and 80 MPa (☆). Middle, solid symbols: $T = 343$ (left triangles), $T =$ 348 (right triangles), 353 (⬢), 358 (★), and 363 K (pentagons); open symbols: $P = 0.1$ (□), 10 (○), 20 (△), 30 (▽), and 40 MPa (◇). Bottom, solid symbols: $T =$ 348 (right triangles), 353 (⬢), 358 (★), and 363 K (pentagons); open symbols: $P = 0.1$ (□), 10 (○), 20 (△), 30 (▽), 40 (◇), 50 (left triangles), 60 (right triangles), and 70 MPa (⬡).

corresponds to the ratio $\Delta E^{\#}/\Delta H^{\#}$,ignoring the small term $RT/2$. The effects of (T,P,V) on the relaxation time, τ, have been recently considered in one theoretical framework by deriving the canonical set of equations.[33]

In discussing the origin of the dynamic processes in p*t*BA and pODMA, knowledge of the equation of state is necessary. The PVT results for the same p*t*BA as the one used in the DS and rheology studies ($M_n = 82\,800$ g/mol) can be found in the Supporting Information section (Figure S4). For pODMA, we have employed literature PVT data for the equation of state.[34] In both cases, the Tait equation was employed for fitting the temperature range where the DS experiments were made

$$\begin{aligned} V(P,T) &= V(0,T)(1-0.0894\ln(1+P/B(T))) \\ V(0,T) &= \alpha_0+\alpha_1 T+\alpha_2 T^2 \\ B(T) &= B_0\exp(-B_1 T) \end{aligned} \tag{9}$$

Here α_0, α_1, and α_2 are coefficients of thermal expansion and B_0 and B_1 are parameters that describe the T dependence of the compressibility. For p*t*BA, the following Tait parameters were used for temperatures above T_g: $\alpha_0 = 0.87751$ cm^3/g, $\alpha_1 = 2.4 \times 10^{-4}$ cm^3/gK, $\alpha_2 = 6.49 \times 10^{-7}$ cm^3/gK^2, $B_0 =$ 762 MPa, and $B_1 = 5.17 \times 10^{-3}$ K^{-1}.

The $\tau(T, P)$ dependencies together with the (P, V, T) equation-of-state result in the $\tau(T,\rho)$ representation shown in Figure 7 for the α, α′, and ionic processes of p*t*BA. The corresponding density representation for the relaxation times of the segmental process of pODMA at $T > T_m$ is shown in Figure 9 (top). The lines are fits of the modified VFT equation for the density[23] as the independent variable:

$$\tau_{max} = \tau_0 \exp\frac{D_\rho \rho}{\rho_0 - \rho} \tag{10}$$

where $D\rho$ is a dimensionless parameter, τ_0 is the limit of relaxation times at high densities, and ρ_0 is the "ideal glass" density. According to the canonical set of equations, among many different possibilities, the ratio of activation energies, $Q_V(T,V)/Q_P(T,P)$ can be obtained through the $\tau(T,\rho)$ representation from the slopes at the crossing points of the "isothermal" and "isobaric" as[33]

$$\frac{Q_V}{Q_P} = 1 - \frac{(\partial \ln \tau/\partial\rho)_T}{(\partial \ln \tau/\partial\rho)_P} \tag{11}$$

The result of the dynamic ratio for all three processes of p*t*BA is shown in Figure 8. For the α process, the ratio is only weakly dependent on temperature, and its value at $P = 0.1$ MPa and $T \approx T_g$ is ~0.54, suggesting that both density and temperature control the dynamics. Equally small is this ratio for the α′ process (~0.52 near the merging temperature at $P = 0.1$ MPa) (Figure 8, middle). The low value of the ratio of activation energies for the segmental relaxation can be understood on the basis of the large monomeric volume. We have shown[35] that the repeat unit volume and local packing play a key role in controlling the value of this ratio at T_g and thus the dynamics associated with the glass temperature. In particular, for flexible main-chain polymers, temperature, through the presence of energy barriers opposing molecular motions, is the main parameter affecting the dynamics, whereas in polymers with bulky side groups or in glass-forming liquids with large molar volumes, volume effects gain importance. Similar conclusions were reached by recent different approaches.[36,37] Similarly, the relatively low value of the ratio of activation energies for the slow process (Figure 8, bottom) is not surprising because the ion mobility is coupled to the polymer dynamics. The segmental relaxation of pODMA above T_c is controlled primarily by temperature, as indicated by the extremely high values of the

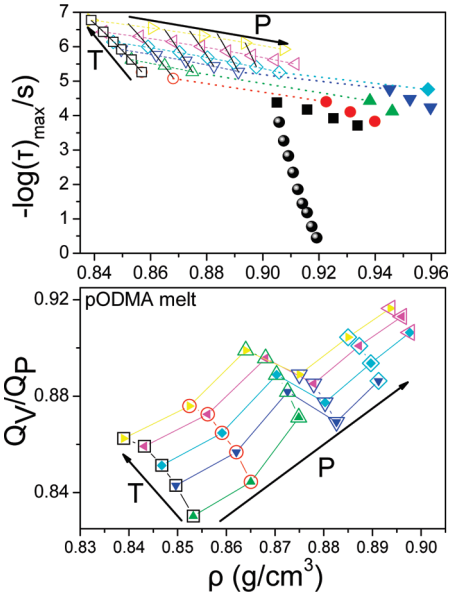

Figure 9. (Top) Segmental relaxation times of pODMA plotted as a function of density. The lines are fits of the modified VFT equation (eq 10); Isothermal: $D_\rho^T = 4.4$ (---, $T = 312$ (●), 321 (▲), 329 (▼), 338 (◆), 303 (left triangles), and 350 K (right triangles)); isobaric: $D_\rho^P = 2.6$ (—, $0.1 < P < 150$ MPa in 30 MPa increments, spheres: $P = 0.1$ MPa). The dotted lines indicate the melting regimes. (Bottom) Variation of the ratio of activation energies Q_V/Q_P on temperature and pressure. Solid symbols: temperatures as above; open symbols: $P = 0.1$ (□), 30 (○), 60 (△), 90 (▽), 120 (◇), and 150 MPa (left triangles).

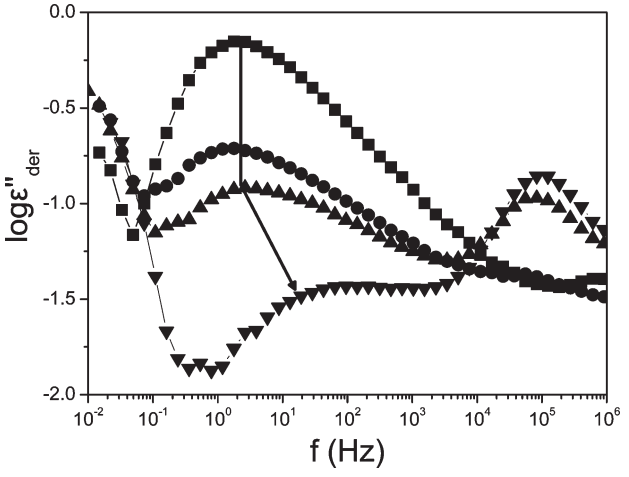

Figure 10. Dielectric loss spectra of p*t*BA (■), S14 (●), S52 (▲), and S81 (▼) at $T = 325$ K. The curves show the speed-up of the p*t*BA segmental relaxation times when this block is confined (S81).

ratio of activation energies (0.83 at atmospheric pressure, Figure 9). This is consistent with the above picture given the high monomer asymmetry; the ethylene-like side group is much longer then the backbone, and this gives rise to segmental dynamics that are dominated by the polyethylene-like side groups where temperature is expected to dominate the dynamics.[38]

Triblock Dynamics. We now turn to the dynamics of the triblock copolymers. Figure 10 gives representative dielectric loss spectra of S14, S52, S81, and the p*t*BA homopolymer at $T = 325$ K. The copolymer loss curves display two peaks, assigned to the segmental relaxation of p*t*BA and pODMA at low and high frequencies, respectively. As is clearly observed, the p*t*BA segmental dynamics in S81 speed up

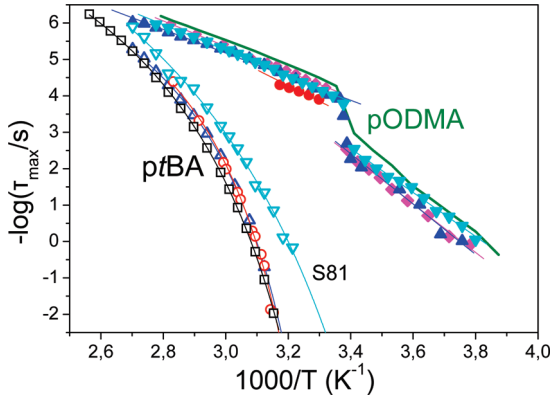

Figure 11. Arrhenius plot of the segmental dynamics corresponding to the p*t*BA and pODMA blocks in the pODMA-*b*-p*t*BA-*b*-pODMA triblock copolymers: bulk p*t*BA (■), S14 (●), S52 (▲), S81 (▼), S94 (◆), and bulk pODMA (green line). Notice the slowing down of the pODMA segmental dynamics upon crystallization and the speed up of the p*t*BA segmental dynamic upon confinement (S81). In the latter, the estimated p*t*BA radius of gyration is comparable to the cylinder radius. (See the text).

when compared with bulk ptBA. The pODMA segmental process remains at about the same frequency in accord with the pODMA homopolymer.

The dielectric loss curves were fitted to a summation of two HN functions (eq 1), and at each temperature, the characteristic relaxation time was obtained for each process. The shape parameters for the p*t*BA block in the copolymers are $m = 0.75 \pm 0.09$, $n = 0.28 \pm 0.09$ (S52) and $m = 0.64 \pm 0.07$, $n = 0.20 \pm 0.03$ (S81). The corresponding parameters for the pODMA block are $m = 0.85 \pm 0.05$, $n = 0.50 \pm 0.05$, and $m = 0.30 \pm 0.02$, $n = 1$ above and below T_c, respectively, for all samples. The dynamic results for the homopolymer and the three copolymers are presented in the Arrhenius representation of Figure 11. All relaxation times reported are from the second cooling run to ensure the same thermal history. The relaxation times of the p*t*BA block in the copolymers follow consistently a strong T dependence, as with the respective homopolymer. The $\tau(T)$ of this process can be described by the same VFT parameters for S14 and S52, using $T_0 = 272 \pm 1$ K, $\tau_0 = (6.0 \pm 0.5) \times 10^{-12}$ s, and $D_T = 5.0 \pm 0.1$. In contrast with this, the p*t*BA segmental dynamics in S81 speed up by about half a decade at high temperatures and as much as two decades in the vicinity of the respective glass temperature. The VFT parameters now change to $T_0 = 261 \pm 1$ K and $\tau_0 = (1.4 \pm 0.5) \times 10^{-11}$ s, whereas D_T remains the same. As a result, the thus obtained T_g (303 K) is lower than that in the p*t*BA homopolymer. The relaxation times corresponding to the pODMA block relaxation in S14, S52, S81, S94, and pure pODMA exhibit an Arrhenius temperature dependence (eq 5) with an apparent activation energy, E, of 63.5 ± 0.8 and 135 ± 2 kJ/mol in the liquid and the crystal phases, respectively (high temperature intercepts of $\tau_0 \approx 10^{-15}$ and 10^{-24} s, respectively). The $\tau(T)$ displays the characteristic discontinuity at the transition temperature, T_c. In addition, T_c, is only slightly affected from the triblock composition except for the S14. We shall discuss this point later together with the high-pressure results.

Next, we investigate the pressure dependence of the glass temperature and of the crystallization temperature corresponding to the amorphous (p*t*BA) and crystallizable (pODMA) blocks. Increasing pressure above a critical value, P_c, induces the side-group crystallization in pODMA under isothermal conditions. The signature of crystallization is the

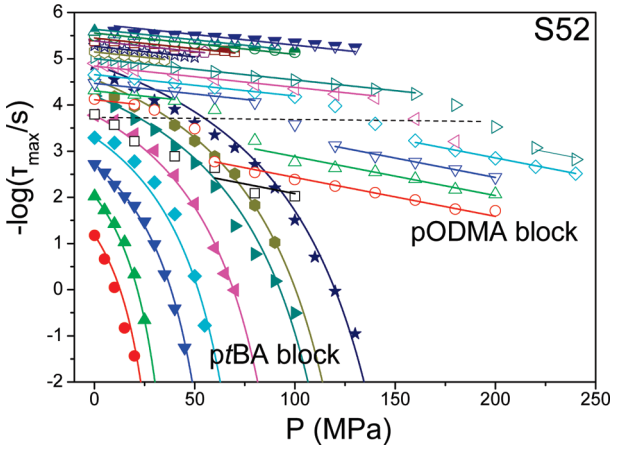

Figure 12. Segmental relaxation times in the S52 triblock copolymer as a function of pressure at different temperatures: p*t*BA block (filled symbols); T = 323 (■), 328 (●), 333 (▲), 338 (▼), 343 (◆), 348 (left triangles), 353 (right triangles), 358 (⬢), and 363 K (★). The data have been fitted with the modified VFT equation for the pressure dependence. The respective relaxation times for the pODMA block (open symbols) are: T = 298 (□), 303 (○), 308 (△), 313 (▽), 318 (◇), 323 (left triangles), 328 (right triangles), 333 (⬡), 338 (☆), 343 (⌂), 348 (⬒), 353 (◓), 358 (up triangles (top solid)), and 363 K (down triangles (top solid)). The solid lines represent linear fits to the pODMA times, above and below T_c. The pressure dependence of the crystallization temperature, $T_c(P)$, is denoted with the dashed line.

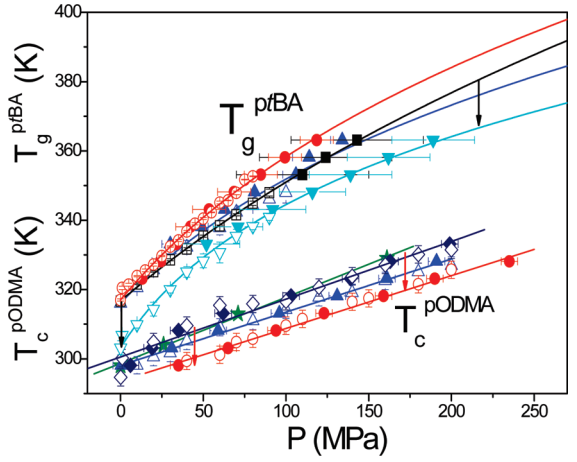

Figure 13. Pressure dependence of the glass temperature of p*t*BA (T_g^{pBA}) and of the crystallization temperature of pODMA (T_c^{pODMA}) in the different triblock copolymers: bulk p*t*BA (■), S14 (●), S52 (▲), S81 (▼), S94 (◆), and pODMA (★); open and filled symbols correspond to data obtained under "isobaric" and "isothermal" conditions, respectively. The solid lines represent the $T_g(P)$ and $T_c(P)$ fits to eq 12 and to the Clausius−Clapeyron equation, respectively. Notice the steeper pressure dependence of T_g^{pBA} (dT_g/dP = 0.41 K·MPa^{-1}) as compared with the T_c^{pODMA} (dT_c/dP = 0.19 K·MPa^{-1}), revealing that pODMA crystallization takes place within a glassy environment (p*t*BA). The effect of confinement, at the two extreme cases, is to decrease the T_g^{pBA} by ∼15 K (in S81) and to decrease the T_c^{pODMA} (in S14).

loss of intensity and the slower relaxation of dipoles within the so-called "restricted amorphous phase" (RAP).[39,40,13] The pressure dependence of the relaxation times of the two blocks under "isothermal" conditions is shown in Figure 12 for the representative case of S52. The slower process, corresponding to the p*t*BA block segmental relaxation, follows a VFT dependence for all temperatures in the range of $323 < T < 363$ K, described by the pressure equivalent of VFT (eq 6) with (D_P = 6.6). The corresponding relaxation times for the pODMA block, for temperatures in the range $298 < T < 363$ K, display an Arrhenius T-dependence both below and above $T_c(P)$. The characteristic crystallization pressure was extracted for each isotherm from the discontinuous change of $\tau(P)$ (obtained by estimating the intermediate pressure between the highest pressure of the liquid phase and the lowest pressure of the crystal phase, for each temperature) (dashed line in Figure 12).

Figure 13 presents the true, that is, thermodynamic $T(P)$ phase diagram from the four copolymers investigated. The diagram contains the $T_g^{pBA}(P)$ and $T_c^{pODMA}(P)$ dependencies of the respective blocks in the copolymers as well as in the homopolymers. The open symbols are extracted from the "isobaric" measurements, whereas the filled symbols are from the "isothermal" measurements. Evidently, the pressure dependencies of the glass and crystallization temperatures are drastically different. Even more, surprisingly, it is the glass temperature that has the steeper initial P dependence despite the fact that is not a true thermodynamic transition. Usually, transitions of first-order, such as polymer crystallization (following the Clausius−Clapeyron equation, $dP/dT_m = \Delta H/T\Delta V$, where ΔH is the heat of fusion and ΔV is the associated volume change) are the ones that show the stronger pressure dependence. The puzzle is solved if we recall that in pODMA, it is only the side groups that crystallize;[13] the backbone and part of the side groups remain outside the crystalline lamellar.

From the individual $T_g^{pBA}(P)$ and $T_c^{pODMA}(P)$ dependencies, we can draw interesting conclusions on the dynamic state of each block. The former can be described by the empirical equation[41]

$$T_g(P) = T_g(0)\left(1+\frac{\nu}{\mu}P\right)^{1/\nu} \qquad (12)$$

where $T_g(0)$ is the glass temperature at atmospheric pressure and μ and ν are fitting parameters. The values of these parameters for the different copolymers are summarized in Table 3. The pODMA crystallization, being first-order, obeys the Clausius−Clapeyron equation. The initial slope of T_g^{pBA} is higher (dT_g/dP = 0.41 K·MPa^{-1}) as compared with the T_c^{pODMA} (dT_c/dP = 0.19 K·MPa^{-1}, Table 3). Because $T_g^{pBA}(P) > T_c^{pODMA}(P)$, pODMA crystallization in the copolymers takes place consistently at lower temperatures than the glass temperature of p*t*BA. As a consequence of the different $T_g(P)$ and $T_c(P)$ dependencies, increasing pressure isothermally results in pODMA crystallization in an environment that is deeper into the glassy state.

Table 3. Parameters of Equation 12 for the $T_g(P)$ as well as the dT_m/dP dependence

sample	$T_g(0)$ (K)	μ (MPa)	ν	$dT_m/dP\|_{P\to 0}$ (K·MPa^{-1})	dT_m/dP (K·MPa^{-1})
p*t*BA	316	720 ± 20	4.3 ± 0.3	0.41	
S14	317	550 ± 20	6.1 ± 0.6	0.50	0.16
S52	316	610 ± 60	7 ± 2	0.50	0.15
S81	303	410 ± 20	9.3 ± 0.6	0.78	0.17
pODMA					0.19

Confinement affects the thermodynamics and subsequently the dynamics of both the crystallizable and the amorphous block. For the pODMA block, we find that confinement within cylindrical domains in the copolymer with the lower pODMA content (S14) results in a decrease in T_c. This is consistent with recent studies of polymer crystallization under confinement;[41] the crystallization of

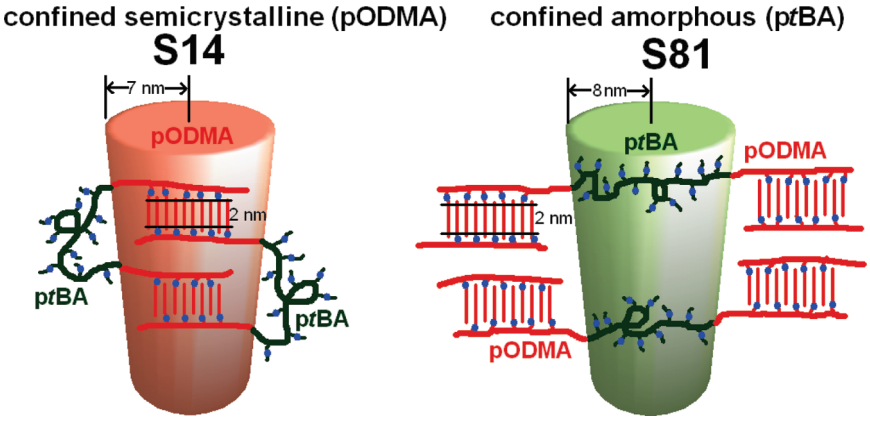

Figure 14. (Left) Schematic representation of the two extreme cases; confinement of the crystallizable block (pODMA, left) within cylinders embedded within the glassy amorphous p*t*BA matrix. (Right) Confinement of the amorphous block (p*t*BA) within cylinders embedded within the pODMA matrix. The blue dots represent the dipoles, situated on the side chains of both polymers.

polyethylene within nanoporous alumina was dominated by nucleation (i.e., lower T_c) and gave rise to a reduced overall crystallinity.[42] In addition, a systematic reduction of T_c (and ΔH) was found in nanophase-separated diblock copolymers of pODMA-*b*-PS that was attributed to the curved interface (cylindrical morphology) that reduces the ability of alkyl chains to crystallize.[43] Furthermore, the glass temperature of the confined p*t*BA in S81 is decreased by ~15 K over the whole pressure range investigated. This speed-up of dynamics is a manifestation of the confinement of the p*t*BA block within the nanodomains. Notice that the p*t*BA segmental dynamics are faster even at atmospheric pressure (Figures 10 and 11). This feature can be explained if we consider the length scale of confinement. In S81, the minority block forms hexagonally packed cylinders within the pODMA matrix. The cylinder radius is calculated as $R = ((d_0^2/2\pi)\sqrt{3}f)^{1/2}$, where d_0 is the nearest neighbor distance between cylinders ($d_0 = d(4/3)^{1/2}$) given by SAXS ($d_0^{S14} = 36.5$ nm; $d_0^{S81} = 35.0$ nm), and it is equal to 7 and 8 nm for the extreme cases of confined pODMA (S14) and p*t*BA (S81), respectively. This size is comparable to the radius of gyration of the confined block in both cases: Using the data of Fetters et al.[44] for PMMA and PMA (assuming that pODMA and p*t*BA have similar molecular size, respectively), we calculate the radius of gyration to be $\langle R_g^2\rangle = \langle r^2\rangle_0/6$, where $\langle r^2\rangle_0^{pODMA} = M\cdot 0.425$ (Å^2/(g/mol)) and $\langle r^2\rangle_0^{ptBA} = M\cdot 0.436$ (Å^2/(g/mol)), with M being the respective molecular weight (Table 1). The resulting values are $\langle R_g\rangle_{S14}^{pODMA} = 2.9$ nm and $\langle R_g\rangle_{S81}^{ptBA} = 4.2$ nm. The estimated radius of gyration is thus comparable to the cylinder size of the confined phase, and for this reason, confinement has a pronounced effect on the dynamics of the constraint phase. This is in accord with several reports of enhanced mobility when the molecules are confined to dimensions comparable to their sizes.

A schematic representation of the effect of nanoscale confinement for the triblocks with antisymmetric compositions is shown in Figure 14. For low pODMA content (e.g., S14), hexagonally packed pODMA cylinders are embedded within the amorphous p*t*BA matrix. Upon pressurization, p*t*BA undergoes a liquid-to-glass transition, and at more elevated pressures, side-group crystallization of pODMA takes place within a glassy environment. On the other hand, in the copolymers rich in pODMA (e.g., S81), the dynamic structure consists of glassy p*t*BA cylinders surrounded by a mobile pODMA matrix. Increasing pressure results in the crystallization of the matrix.

IV. Conclusions

The temperature and pressure dependence of the segmental relaxation times, investigated with DS, coupled to the equation-of-state identified the main control parameters giving rise to the liquid-to-glass transition in two homopolymers bearing very asymmetric units: poly(*tert*-butyl acrylate) and poly(*n*-octadecyl methacrylate). It was shown that temperature and volume equally influence the segmental dynamics of p*t*BA. In contrast, in pODMA, the segmental dynamics in the melt state are controlled primarily by temperature. This is anticipated by the ethylene-like side group that dominates the monomer unit.

The investigation of the segmental dynamics in the pODMA-*b*-p*t*BA-*b*-pODMA triblock copolymers as a function of temperature and pressure resulted in the true thermodynamic ($T-P$) phase diagram at each composition. It was shown that the glass temperature of the amorphous p*t*BA is consistently higher than the crystallization temperature of the crystallizable pODMA at all temperatures and pressures investigated. Furthermore, for the initial pressure coefficients, it was shown that $(dT_g/dP)_{P\to 0} > (dT_c/dP)_{P\to 0}$. As a consequence, pODMA crystallization in the copolymers under elevated pressures takes place within a p*t*BA environment that is deeper into the glassy phase.

There were two main effects of confinement in the triblocks with the more antisymmetric compositions under conditions where the radius of gyration of the confined block was comparable to the cylinder radius. Confinement of the pODMA block within the cylindrical domains resulted in the depression of the crystallization temperature. Confinement of the p*t*BA block within the cylindrical domains resulted in the speed-up of the segmental dynamics and to a T_g depression by ~15 K. These results demonstrate that the well-controlled nanometer-size nanodomains of block copolymers can be employed for studying the effect of confinement on the thermodynamic and dynamics properties of crystallizable and amorphous blocks.

Acknowledgment. This work was cofinanced by the E.U. European Social Fund (75%) and the Greek Ministry of Development GSRT (25%) in the framework of the program PENED2003 (no. 856). We thank A. Best (MPI-P) for the *PVT* measurements and G. Tsoumanis (UoI) for technical support. Financial support of the Deutsche Forschungsgemeinschaft, SFB 625 is gratefully acknowledged.

Supporting Information Available: Thermal properties, dielectric spectroscopy, apparent activation volume of p*t*BA, p*t*BA equation of state, and references. This material is available free of charge via the Internet at http://pubs.acs.org.

References and Notes

(1) (a) Forrest, J. E.; Jones, R. A. L. In *Polymer Surfaces, Interfaces, and Thin Films*; Karim, A., Kumar, S., Eds.; World Scientific: Singapore, 2000. (b) Forrest, J. A.; Dalnoki-Veress, K. *Adv. Colloid Interface Sci.* **2001**, *94*, 167.
(2) Reiter, G.; Forrest, J. A. *Eur. Phys. J. E* **2002**, *8*, 101–266.
(3) Huwe, A.; Kremer, F. In *Liquid Dynamics: Experiment, Simulation, and Theory*; Fourkas, J. T., Ed.; ACS Symposium Series *820*; American Chemical Society: Washington, DC, 2002; pp 268−283.
(4) Anastasiadis, S. H.; Karatasos, K.; Vlachos, G.; Manias, E.; Giannelis, E. P. *Phys. Rev. Lett.* **2000**, *84*, 915.
(5) Elmahdy, M. M.; Chrissopoulou, K.; Afratis, A.; Floudas, G.; Anastasiadis, S. H. *Macromolecules* **2006**, *39*, 5170.
(6) Sasaki, T.; Shimizu, A.; Mourey, T. H.; Thurau, C. T.; Ediger, M. D. *J. Chem. Phys.* **2003**, *119*, 8730.
(7) Duran, H.; Gitsas, A.; Floudas, G.; Mondeshki, M.; Steinhart, M.; Knoll, W. *Macromolecules* **2009**, *42*, 2881.
(8) Hadjichristidis, N.; Pispas, S.; Floudas, G. *Block Copolymers: Synthetic Strategies, Physical Properties, and Applications*; Wiley-Interscience: Hoboken, NJ, 2003.
(9) Roland, C. M.; Hensel-Bielowka, S.; Paluch, M.; Casalini, R. *Rep. Prog. Phys.* **2005**, *68*, 1405.
(10) (a) Floudas, G. Chapter 8. In *Broadband Dielectric Spectroscopy*; Kremer, F.; Schönhals, A., Eds.; Springer: Berlin, 2002. (b) Floudas, G. *Prog. Polym. Sci.* **2004**, *29*, 1143.
(11) (a) Roland, C. M.; Bogoslovov, R. B.; Casalini, R.; Ellis, A. R.; Bair, S.; Rzoska, S. J.; Czuprynski, K.; Urban, S. *J. Chem. Phys.* **2008**, *128*, 224506. (b) Bogoslovov, R. B.; Roland, C. M.; Czub, J.; Urban, S. *J. Phys. Chem. B* **2008**, *112*, 16008.
(12) (a) Elmahdy, M. M.; Floudas, G.; Mondeshki, M.; Spiess, H. W.; Dou, X.; Müllen, K. *Phys. Rev. Lett.* **2008**, *100*, 107801. (b) Floudas, G.; Mierwza, M.; Schönhals, A. *Phys. Rev. E* **2003**, *67*, 31705.
(13) (a) Mierzwa, M.; Floudas, G.; Štepánek, P.; Wegner, G. *Phys. Rev. B* **2000**, *62*, 14012. (b) Mierzwa, M.; Floudas, G. *IEEE Trans. Dielectrics Electr. Insul.* **2001**, *8*, 359.
(14) (a) Elmahdy, M. M.; Dou, X.; Mondeshki, M.; Floudas, G.; Butt, H.-J.; Spiess, H. W.; Müllen, K. *J. Am. Chem. Soc.* **2008**, *130*, 5311. (b) Elmahdy, M. M.; Mondeshki, M.; Dou, X.; Butt, H.-J.; Spiess, H. W.; Müllen, K.; Floudas, G. *J. Chem. Phys.* **2009**, *131*, 114704.
(15) Mpoukouvalas, K.; Floudas, G.; Verdonck, B.; Du Prez, F. E. *Phys. Rev. E* **2005**, *72*, 011802.
(16) Wu, W.; Huang, J.; Jia, S. J.; Kowalewski, T.; Matyjaszewski, K.; Pakula, T.; Gitsas, A.; Floudas, G. *Langmuir* **2005**, *21*, 9721.
(17) Matyjaszewski, K.; Xia, J. H. *Chem. Rev.* **2001**, *101*, 2921.
(18) Matyjaszewski, K.; Patten, T. E.; Xia, J. H. *J. Am. Chem. Soc.* **1997**, *119*, 674.
(19) Qin, S. H.; Saget, J.; Pyun, J. R.; Jia, S. J.; Kowalewski, T.; Matyjaszewski, K. *Macromolecules* **2003**, *36*, 8969.
(20) Mierzwa, M.; Floudas, G.; Wegner, G. Effect of Pressure on the Side-Chain Crystallization of Poly(*n*-octadecyl methacrylate) Studied by Dielectric Spectroscopy. *Dielectrics Newsletter*, June 2000, pp 1−4.
(21) Havriliak, S.; Negami, S. *Polymer* **1967**, *8*, 161.
(22) Richert, R.; Wagner, H. *Solid State Ionics* **1998**, *105*, 167.
(23) Papadopoulos, P.; Peristeraki, D.; Floudas, G.; Koutalas, G.; Hadjichristidis, N. *Macromolecules* **2004**, *37*, 8116.
(24) Steeman, P. A. M.; van Turnhout, J. *Macromolecules* **1994**, *27*, 5421.
(25) Davis, K. A.; Charleux, B.; Matyjaszewski, K. *J. Polym. Sci., Part A: Polym. Chem.* **2000**, *38*, 2274.
(26) Wind, M.; Graf, R.; Heuer, A.; Spiess, H. W. *Phys. Rev. Let.* **2003**, *91*, 155702.
(27) Mpoukouvalas, K.; Gomopoulos, N.; Floudas, G.; Herrmann, C.; Hanewald, A.; Best, A. *Polymer* **2006**, *47*, 7170.
(28) Paluch, M.; Patkowski, A.; Fischer, E. W. *Phys. Rev. Lett.* **2000**, *85*, 2140.
(29) Angell, C. A. *Science* **1995**, *267*, 1924. Stillinger, F. H. *Science* **1995**, *267*, 1935.
(30) Cohen, M. H.; Grest, G. S. *Phys. Rev. B* **1979**, *20*, 1077.
(31) Pakula, T. *J. Mol. Liq.* **2000**, *86*, 109.
(32) Williams, G. *Trans. Faraday Soc.* **1964**, *60*, 1548.
(33) Mpoukouvalas, K.; Floudas, G.; Williams, G. *Macromolecules* **2009**, *41*, 1552.
(34) Rogers, S. S.; Mandelkern, L. *J. Phys. Chem.* **1957**, *61*, 985.
(35) Floudas, G.; Mpoukouvalas, K.; Papadopoulos, P. *J. Chem. Phys.* **2006**, *124*, 074905.
(36) Dudowicz, J.; Freed, K. F.; Douglas, J. F. *J. Chem. Phys.* **2005**, *123*, 111102.
(37) Ngai, K. L.; Roland, C. M. *Macromolecules* **1993**, *26*, 6824.
(38) Bharadwaj, R. K.; Boyd, R. H. *J. Chem. Phys.* **2001**, *114*, 5061.
(39) Huo, P. T.; Cebe, P. *Macromolecules* **1992**, *25*, 902.
(40) Nogales, A.; Ezquerra, T. A.; García, J. M.; Baltá-Calleja, F. J. *J. Polym. Sci., Part B: Polym. Phys* **1999**, *37*, 37.
(41) Andersson, S. P.; Andersson, O. *Macromolecules* **1998**, *31*, 2999.
(42) (a) Shin, K.; Woo, E.; Jeong, Y. G.; Kim, C.; Huh, J.; Kim, K.-W. *Macromolecules* **2007**, *40*, 6617. (b) Woo, E.; Huh, J.; Jeong, Y. G.; Shin, K. *Phys. Rev. Lett.* **2007**, *98*, 136103.
(43) Hempel, E.; Budde, H.; Höring, S.; Beiner, M. *Lect. Notes Phys.* **2007**, *714*, 229.
(44) Fetters, L. J.; Lohse, D. J.; Richter, D.; Witten, T. A.; Zirkel, A. *Macromolecules* **1994**, *27*, 4639.